# Stress-Alteration Enhancement of the Reactivity of Aluminum Nanoparticles in the Catalytic Decomposition of *exo*-Tetrahydrodicyclopentadiene (JP-10)

Souvick Biswas, Dababrata Paul, Nureshan Dias, Kallista Kunzler, Musahid Ahmed,* Michelle L. Pantoya,* and Ralf I. Kaiser*

Read Online

ACCESS | Metrics & More | Article Recommendations | Supporting Information

**ABSTRACT:** High-energy-density aluminum nanoparticles (AlNPs) upon thermal annealing followed by superquenching result in elevated stress levels in the metallic core and reduced surface energy at the core—shell interface. Isomer-selective vacuum ultraviolet-based photoionization mass spectrometry coupled to a high-temperature chemical microreactor reveals that these stress-altered AlNPs (SA-AlNPs) exhibit distinctive temperature-dependent reactivities toward catalytic decomposition of the hydrocarbon jet fuel *exo*-tetrahydrodicyclopentadiene (JP-10, $C_{10}H_{16}$) compared to untreated AlNPs (UN-AlNPs). SA-AlNPs show a delayed initiation of the decomposition for JP-10 by 200 K relative to the UN-AlNPs; however, the full decomposition is achieved at a 100 K lower temperature. Furthermore, there are fewer oxygenated products that are generated from the alumina surface-induced heterogeneous oxidation process and a larger fraction of closed- and open-shell hydrocarbons. Chemical insight bridging the reactivity order of SA-AlNPs at low and high temperatures, simultaneously, is obtained via a detailed examination of the product branching ratios obtained in this study.
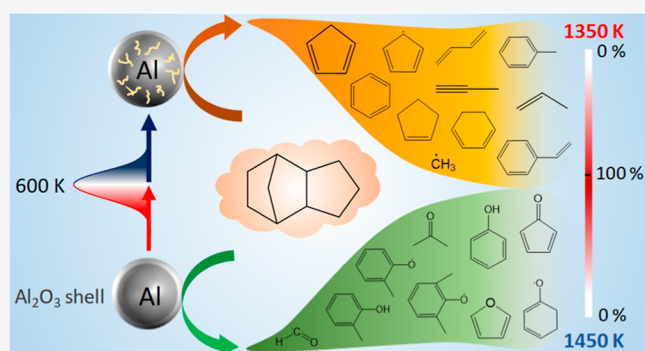
## 1. INTRODUCTION

Aluminum nanoenergetic materials have been the most commonly used nanometallic fuel additives in propulsion and pyrotechnic applications owing to their high gravimetric ($32 \ kJ \ g^{-1}$) and volumetric energy densities ($84 \ kJ \ cm^{-3}$) along with their affordability.[1−7] Aluminum nanoparticles (AlNPs) in particular are often employed as an efficient additive to single component hydrocarbon jet fuels, e.g., *exo*-tetrahydrodicyclopentadiene (JP-10, $C_{10}H_{16}$)[8] in order to achieve enhanced performance of volume-limited air-breathing propulsion systems.[9−21] Considering the enhanced specific surface areas of AlNPs, mass diffusion rates are increased, leading to reduced ignition delays, ultimately elevating the volumetric energy densities of traditional hydrocarbon fuels ($35−40 \ kJ \ cm^{-3}$).[14,15]

Lately, there have been efforts to harness the maximum chemical potential energy available in these NPs, leaving no unburnt fraction, which could affect combustion efficiency.[22−25] The goal is to increase the rate of the reactions associated with AlNPs to achieve greater power. A convenient way to achieve enhanced power output is to alter the properties of these NPs by inducing thermomechanical stresses that also change particle surface energy.[26−31] Usually, the metallic core of the alumina ($Al_2O_3$)-coated AlNPs exists under tensile stress at room temperature. However, when the

temperature is raised to about 673 K, the particle stresses relax.[32] Fast quenching of these AlNPs leads to significant dilatational lattice strain along with an increase in overall stress at the core—shell interface along with lowered surface energy; ultimately, the overall reactivity of the AlNPs is enhanced. Generally, the aluminum core serves as the primary reactant in the combustion reactions, whereas the "inactive" alumina shell inhibits diffusion—oxidation reactions within the core.[33−35] However, recently, an active participation of the shell with the hydrocarbon fuel molecule in the absence of molecular oxygen has been revealed, initiating a low-temperature (650 K) heterogeneous oxidation reaction.[36] This has fundamental implications for accelerating the rate of reactions by providing surface reactions that also promote aluminum-core reaction pathways. In other words, the alumina shell is no longer an "inactive" barrier for reaction, instead an active, exoergic contributor to the generated chemical energy.
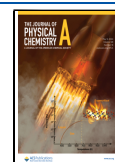
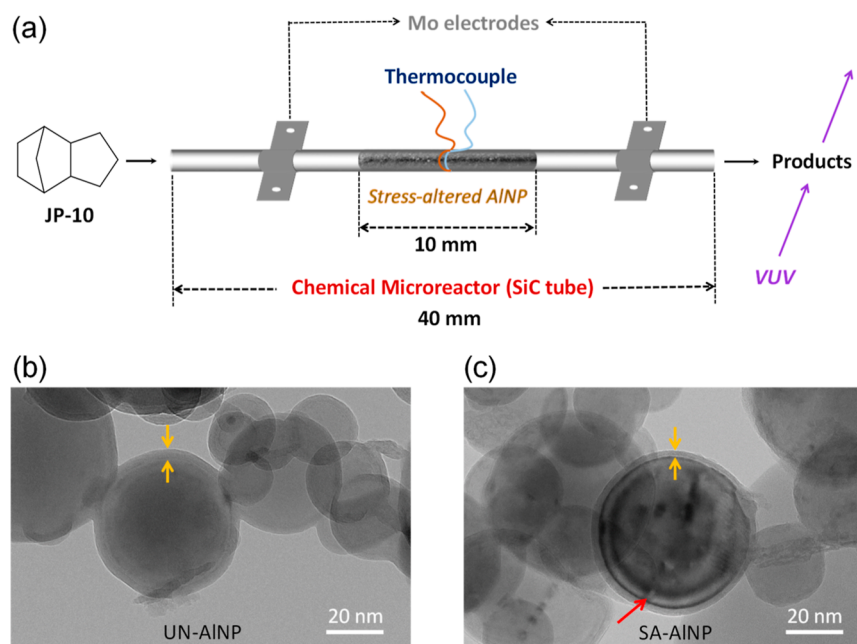**Scheme 1. (a) Catalytic Decomposition of JP-10 Vapor through a Compact Packing of SA-AlNPs in a High-Temperature Chemical Microreactor**[d]



[d]The transmission electron microscopy images of the (b) UN- and (c) SA-AlNPs are also presented, showing the alumina shell (marked with the pair of yellow arrows) and delamination (marked with the red arrow) in the core−shell boundary for the latter.

To assess and understand the performance and specific reactivity of AlNP/JP-10 mixed fuels utilizing both the untreated (UN) and stress-altered (SA) AlNPs, it is necessary to decipher the native molecular interaction with the fuel (JP-10) as a function of the thermal energy of the system. Surface reactions are dependent upon the chemical as well as physical properties of the AlNPs in different temperature regimes. Therefore, the catalytic roles of these AlNPs on JP-10 and their efficiencies could be addressed only by accumulating exhaustive product inventories (including radicals), followed by the quantification of branching ratios, information that is missing to date. The radical species, in particular, drive the oxidation of JP-10 at a later stage, thus controlling the overall efficiency and performance of combustion. Here, we report a substantial alteration in the temperature-dependent intrinsic reactivity of alumina-coated AlNPs upon stress-inducing pretreatment during the catalytic thermal decomposition of JP-10 at combustion-relevant temperatures employing isomer-selective identification of the nascent decomposition products in a chemical microreactor (Scheme 1). The contrasting nature of reactivities between the two kinds of AlNPs in different temperature domains is revealed from the distinct characteristic temperatures of the processes and their respective product distribution.

## 2. METHODOLOGY

### 2.1. Stress-Alteration Treatment of the Aluminum Nanoparticles.
The AlNPs are processed by a thermal annealing and quenching treatment,[26] where the nanopowder is loaded into a sealed container instrumented with a temperature sensor to record powder temperatures during the procedure. The sealed container is then placed in a furnace and heated to 600 K at a rate of 10 K min$^{-1}$, followed by holding for 20 min to allow the annealing conditions to relax residual stresses. After removing the container from the

furnace, it is placed into a liquid quenching solution (a mixture of water, soap, surfactant, and sodium chloride) designed to rapidly reduce the powder temperature to ambient—referred to as superquenching. This pretreatment produces AlNPs with about 40% elevated stress, specifically increasing the stress at the core−shell boundary from −0.191 to −0.380 GPa, with significant delamination (∼80% delamination between the core and shell)[31] and reduced surface energy up to 40%.[37] Both the UN and pretreated AlNP samples have a "passivation" layer of aluminum oxide (Al$_2$O$_3$) around the reactive metallic aluminum core (Scheme 1); hence, they are suitable to preserve and use under atmospheric conditions.

### 2.2. Details of the Catalytic Microreactor.
The nascent gas-phase products formed in the thermal decomposition of helium-seeded *exo*-tetrahydrodicyclopentadiene (JP-10, C$_{10}$H$_{16}$) vapor through the SA-AlNP packing at distinct temperatures from 300 K to 1350 K through the chemical microreactor[36,38−40] (Figure S1) are detected in situ by using single-photon vacuum ultraviolet (VUV) photoionization (PI) mass spectrometry.[39,41] The experiments were carried out at the Chemical Dynamics Beamline (9.0.2.) installed in the Advanced Light Source (ALS) (Figure S1).

In brief, the microreactor was a resistively heated silicon carbide (SiC) tube of 20 mm length and 1 mm inner diameter, which was tightly packed with SA-AlNPs of about a length of 10 mm inside the SiC tube. Ultimately, the packing was done in such a way that the interaction and residence time of the fuel with the NP surface were maximized for optimum reactivity. A gas mixture at a pressure of 500 Torr with JP-10 (TCI America; 94%) in helium carrier gas (He; Airgas; 99.999%) was prepared by bubbling helium gas through JP-10 kept in a stainless-steel bubbler at 298 K. The gas mixture was introduced into the SiC tube where the temperature can reach up to 1600 ± 20 K as monitored by a type-C thermocouple.

After exiting the reactor, the molecular beam containing the pyrolysis products passed a skimmer and entered a detection chamber, which housed the Wiley−McLaren reflectron time-of-flight mass spectrometer. The products were photoionized in the extraction region of the spectrometer by exploiting synchrotron quasicontinuous tunable VUV light from the Chemical Dynamics Beamline 9.0.2 and detected with a microchannel plate detector. Compared to "hard" electron impact ionization, "soft" VUV-PI has the unique advantage of an ideally fragment-free ionization of the neutrals. Further, by tuning the VUV energy, structural isomers can be identified.

Here, mass spectra were recorded in 0.05 eV intervals from 8.00 to 11.50 eV. A set of additional mass spectra was also measured at 15.4 eV to determine hydrogen and methane yields having ionization energies of 15.4 and 12.6 eV, respectively, which cannot be ionized below 11.5 eV. The photoionization efficiency (PIE) curves, which report the intensity of a single mass-to-charge ratio ($m/z$) versus the photon energy, were extracted by integrating the signal collected at a specific $m/z$ selected for the species of interest over the range of photon energies in 0.05 eV increments and normalized to the incident photon flux. The PIE curves were then fitted with a linear combination of known PIE curves to isomer-selectively identify the products. The residence time of JP-10 in the reactor tube (20 mm) under our experimental conditions is tens of ms. This would result in typically three to four (1400 K) collisions of a JP-10 molecule with the helium atoms in the reactor at 500 Torr. However, as the pressure drops from 500 Torr to a few Torr at the exit of the reactor, the actual number of collisions is about one on average.

## 3. RESULTS AND DISCUSSION

**3.1. Mass Spectra.** Figure 1 displays characteristic mass spectra recorded at a photon energy of 10.0 eV at definite intervals in the experimental temperature range. At 300 K, the mass spectrum depicts only three peaks; the most intense one belongs to the molecular parent ion at $m/z = 136$ ($C_{10}H_{16}^{+}$), followed by the weak features of its $^{13}C$ counterpart at $m/z = 137$ ($^{13}CC_9H_{16}^{+}$) and the helium ion at $m/z = 4$. The carrier gas helium is ionized by the traces of high-energy photons from the synchrotron radiation, which could not be filtered out completely from the desired excitation beam.

The first appearance of the product peaks occurs at 850 K in the form of 12 additional mass-to-charge ratios at $m/z = 29$, 41, 54, 66, 67, 68, 78, 79, 80, 82, 94, and 95. The number of mass peaks increases with the rise of the temperature to 1350 K, whereas the parent JP-10 ion count also decays; the latter is barely visible at 1350 K. Molecular mass growth processes beyond JP-10 are absent as no signal exceeding 136 ($C_{10}H_{16}^{+}$) and 137 ($^{13}CC_9H_{16}^{+}$) is detected, suggesting only primary products are detected in the decomposition of JP-10 in our setup. The JP-10 decomposition ratio curves as a function of temperature are shown in Figure 2 to map the efficiency of the SA-AlNPs compared to that of the UN-AlNPs and also in the absence of NPs. The decomposition ratio is defined as the ratio of the decomposed fuel to the intact fuel amount, implying that the full consumption of fuel represented as unity and zero indicates no reaction. The presence of AlNPs results in significant earlier onsets of decomposition of JP-10−650 and 850 K for the UN (blue trace) and SA NPs (red trace), respectively, while decomposition initiates at 1200 K (black trace) in the absence of any catalyst.[36,39] A closer inspection reveals that the patterns in the decomposition curves for UN-
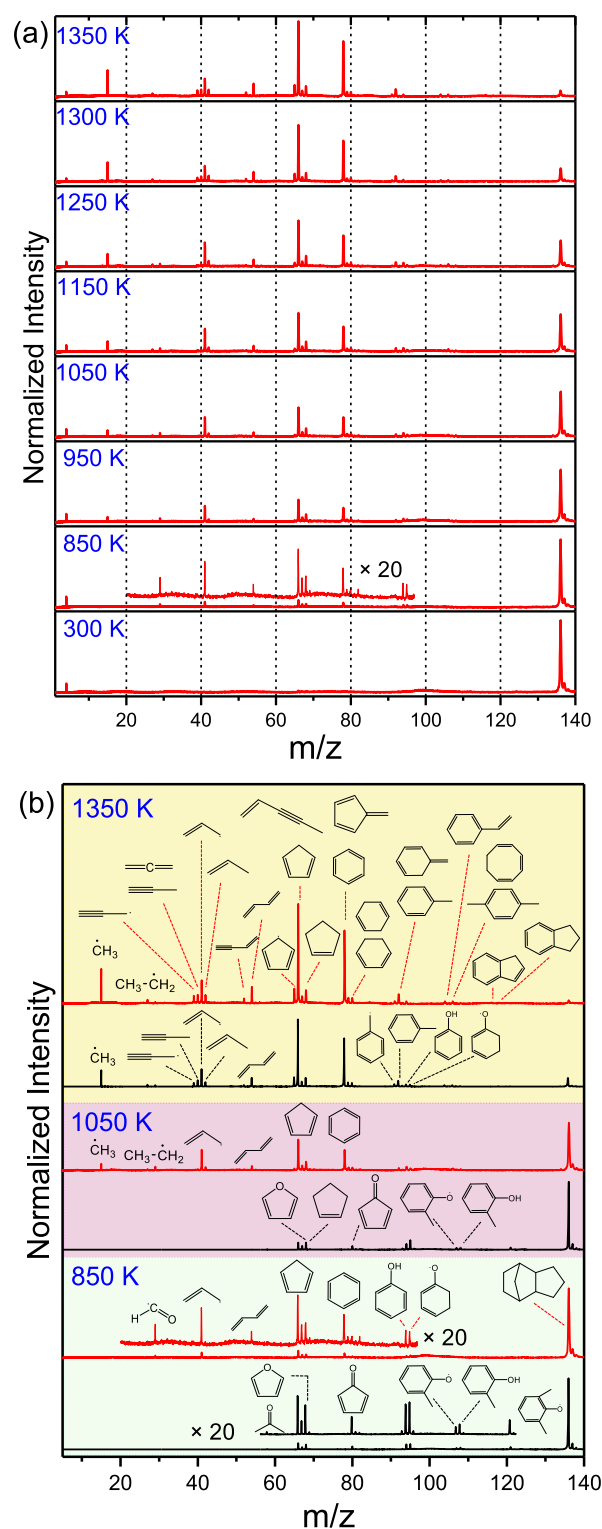


Figure 1. (a) Evolution of mass spectra consisting of the product peaks as a function of temperature formed upon thermocatalytic decomposition of JP-10 through a packing of SA-AlNPs recorded at a photon energy of 10.0 eV in the 300−1350 K temperature range. The peaks, magnified 20 times, within the mass range 20−95 amu are depicted in the inset of the mass spectrum obtained at 850 K. (b) Comparison of the mass spectra recorded at three distinct temperatures with a PI energy of 10.0 eV for the thermal decomposition of JP-10 through UN- (black traces) and SA-AlNPs (red traces). The molecular structures of the major products identified from the PIE curves (described later) are also depicted.
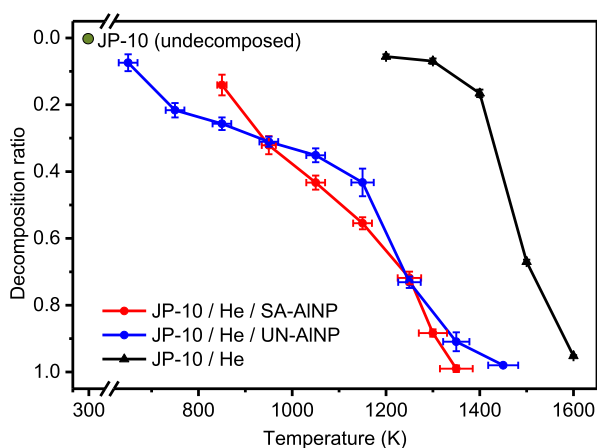
**Figure 2.** Decomposition ratio curves for JP-10 passing through the high-temperature chemical microreactor packed with SA-AlNPs (red trace), UN-AlNPs (blue trace), and without (black trace) AlNPs.

and SA-AlNPs are subtly different. In the former case, two distinct slopes in the ranges of 650−1150 K and 1150−1450 K are noted. However, the SA-AlNPs show a monotonically decaying curve originating around 850 K with a rise in temperature. The quantitative decomposition of JP-10 is lowered by 100 and 250 K in the presence of UN- and SA-AlNPs, respectively, compared to the marked temperature of 1600 K for the gas-phase thermal decomposition. Here, stress-alteration treatment of the AlNPs leads to two notable outcomes in the decomposition curves: first, an increase of the initial decomposition temperature by 200 K and second, a decrease in the full decomposition temperature by 100 K, implying distinguishable catalytic reactivities as a function of temperature in contrast to the uncatalyzed gas-phase decomposition.

**3.2. PIE Curves of the Products.** To decipher the catalytic effects of the SA-AlNPs at the molecular level, comprehensive knowledge of the nascent products formed in the molecular beam requires a detailed analysis of distinct isomer-selective PIE curves. Overall, the identified products (Table S1, Figure 1) in this study[42−51] belong to the class of closed-shell hydrocarbons, hydrocarbon radicals, and oxygenated species (Figure 3 and Figure 4) including oxygenated radicals. The detection of the oxygenated products in the absence of any external supply of molecular oxygen ensures the active surface chemistry involving the oxygen-atom transfer from the aluminum oxide layer ($Al_2O_3$) to the JP-10 molecule, as observed in the case of the UN-AlNPs.[36]

The extensive PIE curve analysis (Figures 3 and 4, S2−S4) denotes that the most intense mass peaks at the initial decomposition temperature (850 K) belong to 1,3-cyclo-pentadiene ($C_5H_6$, $m/z = 66$) and the allyl radical ($^{\bullet}CH_2−CH=CH_2$, $m/z = 41$), along with the oxygenated species— ethynyloxy radical ($HCCO^{\bullet}$, $m/z = 41$), furan ($C_4H_4O$, $m/z = 68$), and the formyl radical ($HCO^{\bullet}$, $m/z = 29$). Two weak features in the mass spectra at $m/z = 94$ and 95 correspond to the oxygenated species: phenol ($C_6H_5OH$) and the 1,3-cyclohexadienyloxy radical ($C_6H_7O^{\bullet}$). At an intermediate temperature of 1050 K, additional peaks appear—especially with smaller hydrocarbon radicals and molecules (C1−C5 systems) such as methyl ($^{\bullet}CH_3$, $m/z = 15$), vinyl ($^{\bullet}CH=CH_2$, $m/z = 27$), propargyl ($^{\bullet}CH_2−C\equiv CH$, $m/z = 39$), cyclo-pentadienyl radical ($^{\bullet}C_5H_5$, $m/z = 65$), acetylene ($HC\equiv CH$,

$m/z = 26$), and ethylene ($H_2C=CH_2$, $m/z = 28$). The C7−C9 hydrocarbons like toluene ($C_7H_8$), styrene ($C_8H_8$), and p-xylene ($C_8H_{10}$), along with additional oxygenated species, i.e., phenoxy radical ($C_6H_5O^{\bullet}$), 2-cyclohexene-1-one ($C_6H_8O^{\bullet}$), and methylphenoxy radical ($CH_3C_6H_4O^{\bullet}$), are also identified.

Raising the temperature to 1350 K results in a complete decomposition of JP-10 and an enhancement of the product yield, specifically for the closed- and open-shell hydrocarbons, such as 1,3-cyclopentadiene ($C_5H_6$, $m/z = 66$), fulvene and benzene ($C_6H_6$, $m/z = 78$), methyl ($^{\bullet}CH_3$, $m/z = 15$), allyl radical ($^{\bullet}CH_2−CH=CH_2$, $m/z = 41$), etc. Although most of the oxygenated species have been identified from the PIE curves, their mass peak intensities tend to be very weak. To ensure comprehensive product detection, mass spectra are also recorded at 15.4 eV (Figure S5), which revealed molecular hydrogen ($H_2$, IE = 15.4 eV),[52] water ($H_2O$, IE = 12.6 eV),[53] and methane ($CH_4$, IE = 12.6 eV)[54] as the products at high temperatures exceeding 1250 K. Figure 5 depicts a compilation of the major products formed throughout the heating temperature range (850−1350 K) of the study based on the mass spectra and PIE curve analysis.

**3.3. Trends in the Relative Abundances of the Products as a Function of Temperature.** The relative abundances of the products probed by measuring the individual mass peak intensities corresponding to different temperatures reveal a sharp increase in the intensities for the closed-shell hydrocarbons and radicals (Figures S6 and S7) as the temperature is raised. Conversely, the trend for oxygenated products shows a bell-shaped curve (Figure S8). The highest values occur between 950 and 1050 K; there is a notable decline beyond 1050 K. This decline is particularly evident for mass peaks that do not solely originate from hydrocarbon molecules or radical species. For instance, the mass peak at $m/z = 41$, which originates from ethyloxy and allyl radicals, exhibits a complex pattern. In contrast to the steep rise for hydrocarbons, a limiting effect is also noted for p-xylene ($m/z = 106$) abundance at 1250 K and possibly arises due to its decomposition to form toluene and styrene,[55,56] both of which continue a steep rise even above 1250 K. Significantly, the emergence of hydrocarbon radicals is initiated at 950 K for the SA-AlNPs as compared to 1150 K for the UN-AlNPs (Figure S9). To depict the primary pathways leading to dominant products in a precise quantitative manner, branching ratios are reported next.

**3.4. Temperature-Dependent Product Branching Ratios.** The individual product branching ratios at three distinct temperatures, representing the initiation, intermediate, and full decomposition temperatures for both the thermal decomposition events of JP-10 over SA- and UN-AlNPs (Figure 6) have been evaluated by documenting the mole fraction (concentration) of a particular product.[36,40]

The initial phase reveals significant differences in terms of product distribution between the two cases. For instance, the branching ratios of the predominant oxidation products— phenol (17.5 ± 0.1 versus 4.9 ± 0.7%), 1,3-cyclohexadienyloxy radical (17.9 ± 0.2 versus 3.1 ± 0.6%), 2,4-cyclopentadiene-1-one (11.4 ± 0.1 versus 0.6 ± 0.2%)—have been lowered when compared between UN-AlNPs versus SA-AlNPs, with no larger oxygenated species, e.g., dimethylphenoxy radical and dimethylphenol, detected even at 850 K for the latter. However, smaller oxygenated radicals such as ethynyloxy (4.7 ± 0.4%) and formyl radicals (2.0 ± 0.1%) tend to form exclusively in the SA-AlNPs case—similar to the remarkably
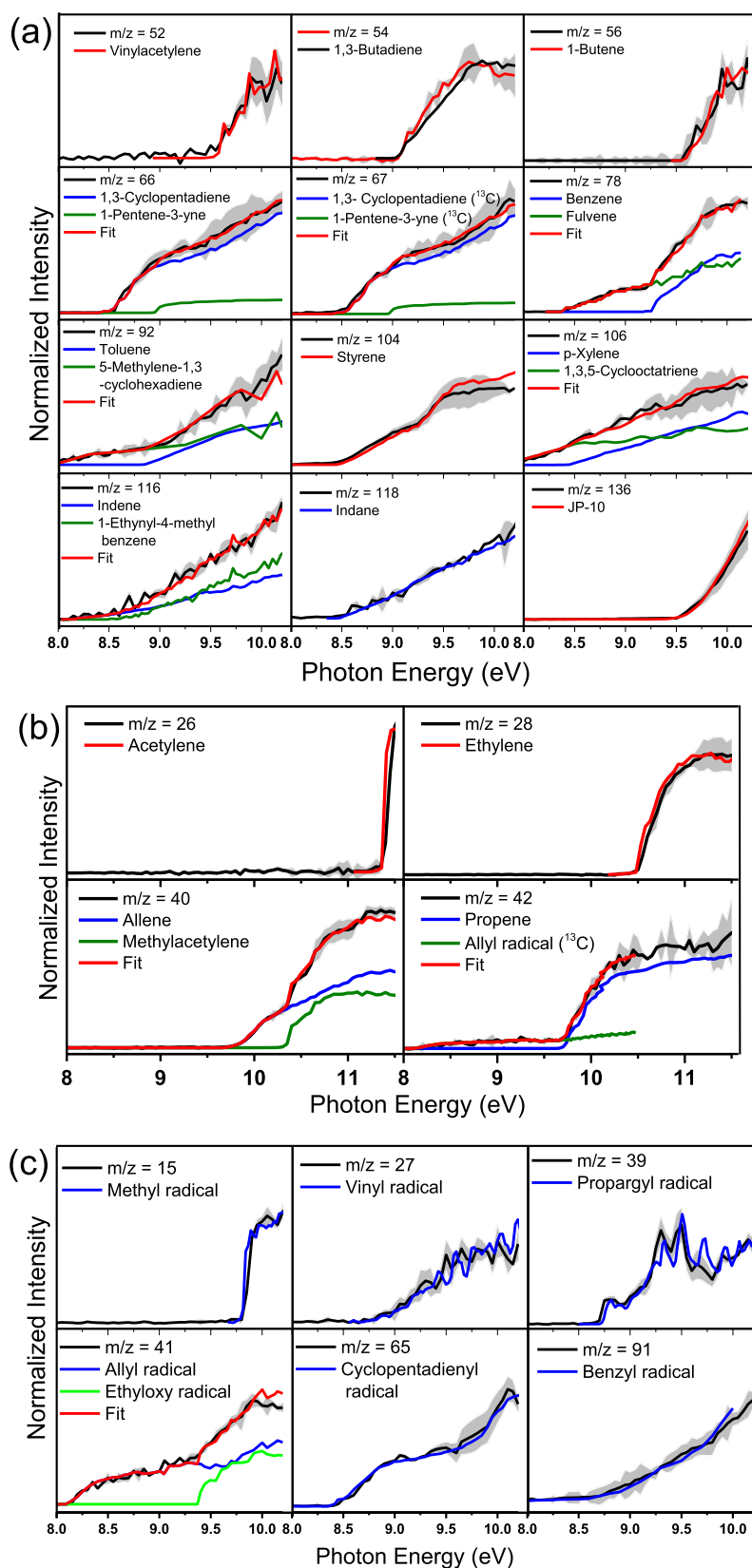
**Figure 3.** Experimental PIE curves (black traces) for the (a,b) closed-shell hydrocarbons (olive and blue reference traces) and (c) radical products (blue reference traces) formed upon catalytic decomposition of JP-10 by the SA-AlNPs along with the experimental errors (gray shaded area) originating from the measurement errors of the photocurrent by the photodiode and a 1-$\sigma$ error of the PIE curves averaged over the individual scans. In case of multiple isomeric contributions, individual reference PIE curves are presented, and the overall fitted curve is depicted by the red trace.

**Figure 4.** Experimental PIE curves (black traces) for the oxygenated products (green reference traces) formed upon thermal decomposition of JP-10 by the SA-AlNPs along with the experimental errors (gray shaded area) originating from the measurement errors of the photocurrent by the photodiode and a 1-$\sigma$ error of the PIE curves averaged over the individual scans. In the case of multiple isomeric contributions, individual reference PIE curves are presented, and the overall fitted curve is depicted by the red trace.
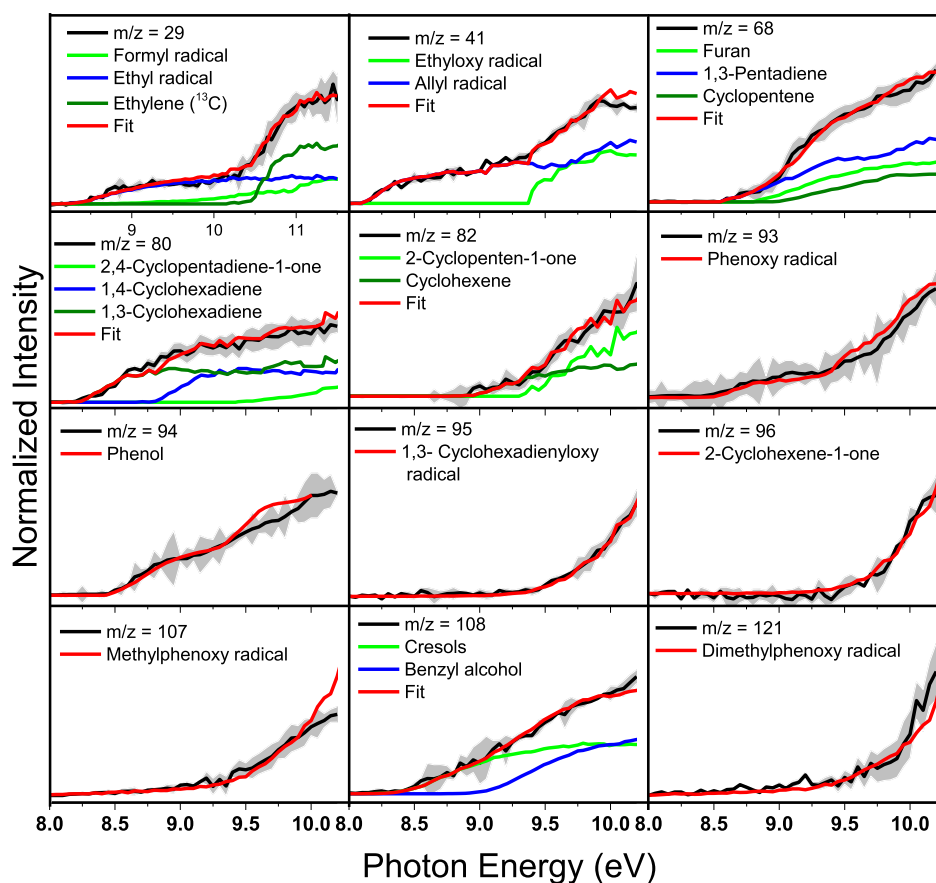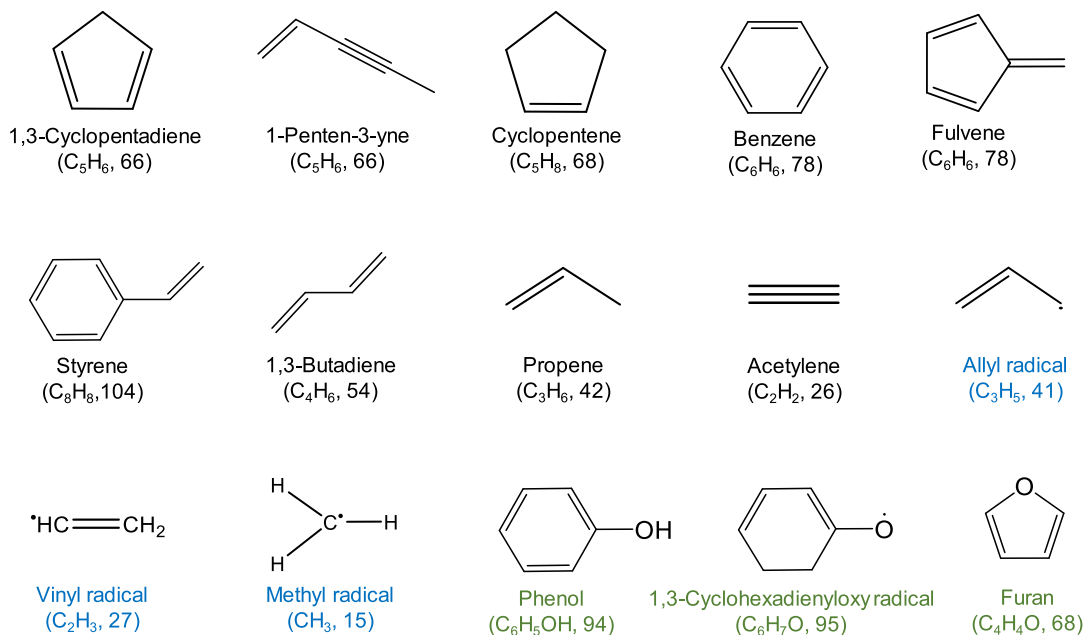


**Figure 5.** Predominantly formed products including closed-shell hydrocarbons, hydrocarbon radicals, and oxygenated species with their corresponding $m/z$ values in parentheses during the thermocatalytic decomposition of JP-10 in the temperature range 850−1350 K by the SA-AlNPs.

enhanced production of the closed-shell hydrocarbon molecules and radicals. Primary 5-carbon thermal decomposition products[40] such as 1,3-cyclopentadiene ($C_5H_6$) and cyclopentene ($C_5H_8$) are unambiguously favored, as evident from

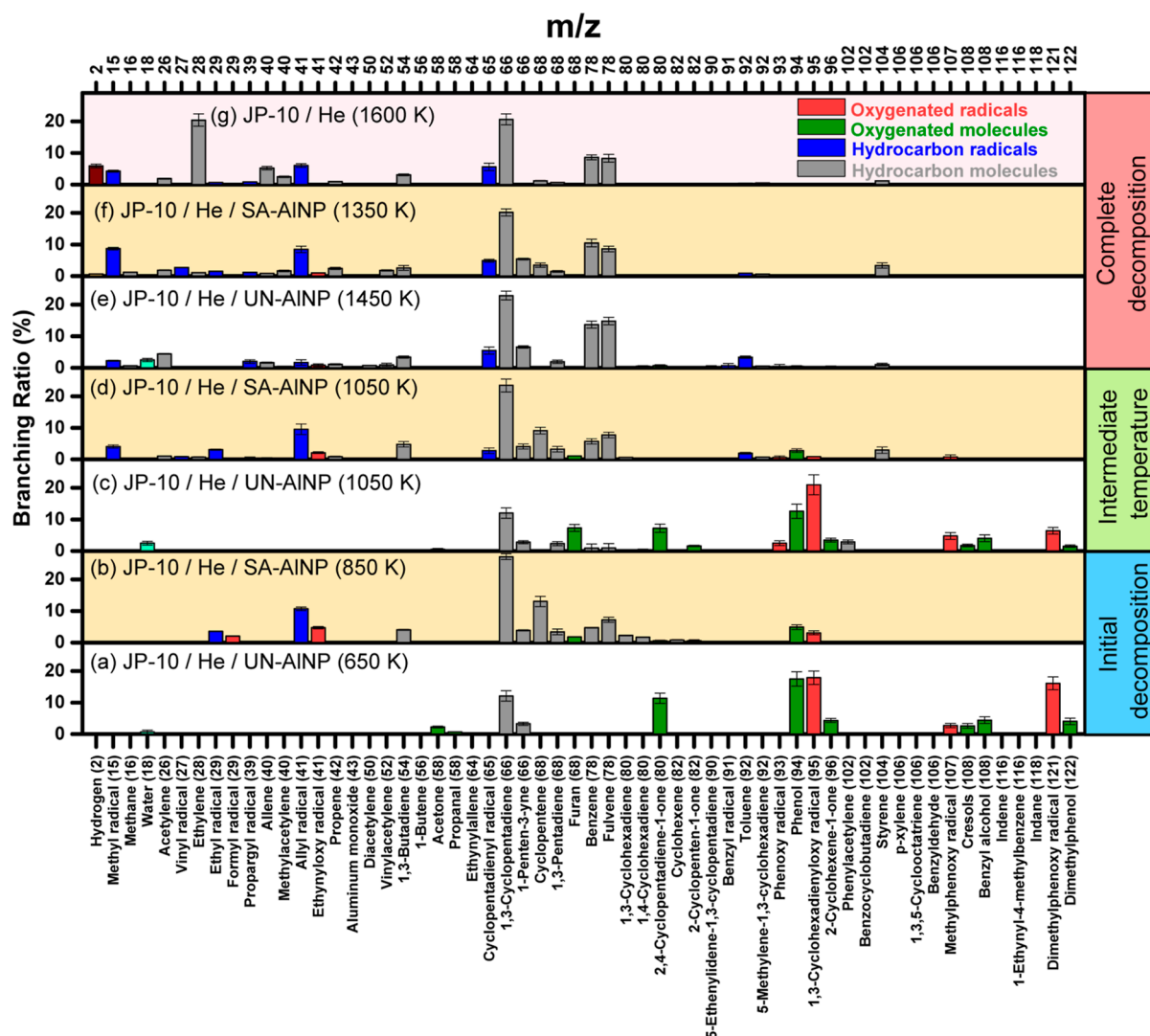**Figure 6.** Individual branching ratios of the species obtained in the thermocatalytic decomposition of JP-10 by SA-AlNPs (shaded area) compared to those of the UN-AlNPs at three respective temperature regions of interest—initial decomposition, intermediate, and complete decomposition of parent JP-10. The product branching ratios for the full decomposition of pure JP-10 is also presented at the top for reference. The error bars are evolved due to the uncertainties determined by averaging the recorded PIE curves.

the branching ratios of 27.2 ± 0.9 and 13.0 ± 0.6%, respectively. Hydrocarbon molecules like fulvene ($C_6H_6$), benzene ($C_6H_6$), 1,3-butadiene ($C_4H_6$), and 1,3-pentadiene ($C_5H_8$) only form at this temperature for SA-AlNPs. At the low-temperature range (650−950 K), there is no significant yield of the open-shell hydrocarbon species in the presence of UN-AlNPs, and the SA NPs yield a noticeable amount of allyl (10.7 ± 0.6%) and ethyl (3.6 ± 0.1%) radicals at 850 K.

At the intermediate temperature (1050 K), the total branching ratio of the oxygenated products combined is much greater than the hydrocarbon products for the UN-AlNPs, revealing the peak of oxygen insertion reaction efficiency.[36] On the contrary, diminished product branching ratios for the oxygenated species at the same temperature are noted for SA-AlNPs; e.g., branching ratios of phenol ($C_6H_5OH$) and 1,3-cyclohexadienyloxy ($C_6H_7O$) radicals have been lowered from 17.5 ± 0.1 to 2.8 ± 0.3% and 17.9 ± 0.2 to 0.9 ± 0.1%, respectively, with the rise in temperature from 850 to 1050 K. However, radicals such as methyl (4.1 ± 0.2%) and cyclopentadienyl (2.8 ± 0.1%) also initially form along with the allyl (9.5 ± 0.8%) and ethyl (3.1 ± 0.2%)

radicals already identified at 850 K, all of which are absent at the identical temperature and conditions using the UN-AlNPs.

The general product distribution patterns look similar in both types of AlNPs and only of the pure JP-10 at the terminal temperatures depicting the complete decomposition (1350, 1450, and 1600 K for SA-AlNPs, UN-AlNPs, and without NPs, respectively) of the parent JP-10. The key common observations for the AlNP cases are the decaying branching ratios for the oxygenated products and the facilitated yield of closed- and open-shell hydrocarbons compared to that of the intermediate temperature (1050 K). The dominant products for all of the events are 1,3-cyclopentadiene, fulvene, and benzene. However, the C1−C3 hydrocarbon molecules and radicals are found to be more abundant for the SA-AlNPs than for the UN NPs, e.g., an increase of branching ratios for allyl (1.7 ± 0.2 to 8.5 ± 0.7%) and methyl (2.2 ± 0.1 to 8.7 ± 0.3%) radicals. On the flipside, the yield of water (∼2%) has been found to be greater for the UN-AlNPs than that of the SA-AlNPs. In the pyrolysis of pure JP-10, additionally, ethylene was found to be one of the most contributing products, indicating extensive fragmentation of the primary decom-

**Scheme 2. Temperature-Dependent Mechanism of Action on the Thermal Decomposition of JP-10 by the (a) SA-AlNPs in Comparison with the (b) UN-AlNPs Involving Different Modes of Predominant Heterogeneous Surface−Gas Phase Reactions**
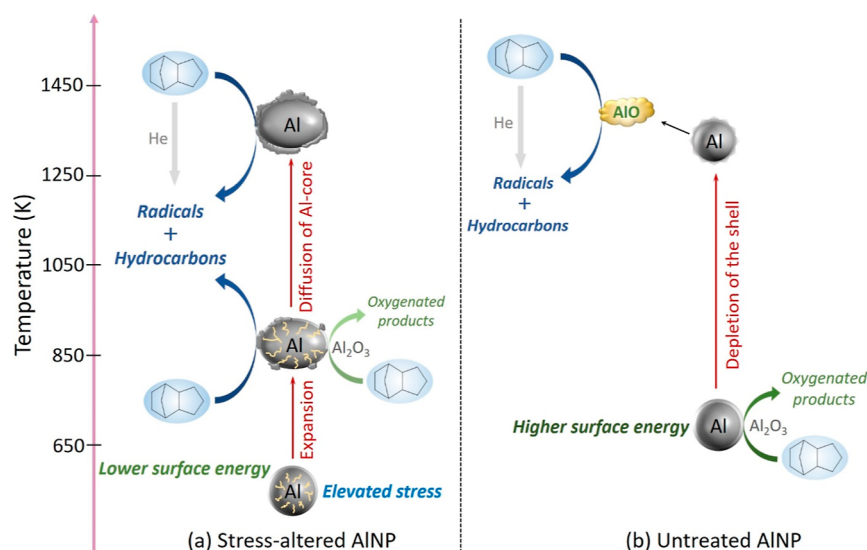


position products in the gas phase due to the excess thermal energy in the microreactor (1600 K).

**3.5. Effects on Reactivity due to Stress-Altering Treatment.** Based on the altered reactivity of the SA-AlNPs in reference to the UN-AlNPs, it is important to understand the temperature-dependent functionalities and native reactive interactions of the NPs toward the JP-10 molecule. The alumina-coated UN-AlNPs revealed a distinct three-stage catalytic role toward the decomposition of JP-10,[36] consisting of a low-temperature heterogeneous oxidation of the fuel on the alumina shell, the generation of aluminum monoxide (AlO) enhancing the primary hydrogen abstraction from the JP-10 molecule at the medium temperature range (1050−1250 K), followed by a simultaneous gas-phase unimolecular thermal decomposition of JP-10 at the high-temperature regime along with the AlO-induced channel. The initiation of the low-temperature decomposition is plausibly driven by a low-energy barrier oxygen insertion step occurring from the oxide shell of AlNPs to the JP-10 molecule. Quantitatively, this step possesses a shortened energy barrier ($\ll 400$ kJ mol$^{-1}$) than that of the homolytic C−H cleavage of pure JP-10 in the gas phase.[40] The monooxygen-substituted JP-10 species then can undergo facile C−C cleavages to produce a hydrocarbon and an oxygenated species, and this justifies their simultaneous emergence.

The initial phase of the decomposition of JP-10 occurs at a 200 K higher temperature for the SA-AlNPs as compared to that of the UN-AlNPs, indicating a slower initial reactivity of the former in the low-temperature regime. This delayed initiation (850 K) for the SA-AlNPs could be directly correlated with the reduced surface energy. The pretreated particles possess an elevated stress level (presented by the yellow curved lines in Scheme 2) due to the change in the metal microstructure and the void shrinkage in the aluminum core,[57] which results in reduced surface energy compared to that of the UN particles. This lowering of the surface energy leads to diminished adhesion of JP-10 molecules, affecting the residence time on the surface, hence producing reduced surface reactivity for the SA-AlNPs at the initial temperatures. The identical order of reduced reactivities has also been observed previously for the preignition reaction at the surface

of SA-Al particles in the presence of molecular oxygen, where Shancita et al. showed that a thicker oxide film was generated for the UN particles, indicating that a greater extent of heterogeneous reaction originated from a higher surface energy compared to that of the SA particles.[37,58]

Given that the low-temperature dissociative oxidation of JP-10 is solely governed by the alumina shell of the AlNPs involving a heterogeneous oxygen atom transfer to the fuel molecule, it thus indicates that the SA-AlNPs do not have the requisite surface energy (or chemical potential) at 650 K, hence providing a less reactive or less energetically favorable alumina surface for the activation of the JP-10 molecule. The initial product formation and their quantitative distribution disclose diminished branching ratios of oxygenated products (80.2 and 17.8% for UN- and SA-AlNPs, respectively), and they decrease with the rise in temperature for the SA-AlNPs, unlike for the UN-AlNPs, where the oxygenated products collectively (including water) exceed the hydrocarbon products up to a temperature of 1050 K. This observation also substantiates the suppressed heterogeneous oxidation chemistry on the alumina shell and indicates other contributing reaction channels through thermocatalytic C−C/C−H bond cleavages, favoring the formation of hydrocarbon molecules and radicals.

The temperature-dependent decomposition profile of JP-10 in the presence of SA-AlNPs depicts a sharp monotonic decay (Figure 2) beyond the initial decomposition phase, suggesting a more efficient catalytic activity for the pretreated AlNPs with an increase in temperature. Bello et al. showed that due to the enhanced tensile stress of the core material for the SA-AlNPs, some delamination occurs at the interface of the crystalline metallic core and amorphous alumina shell, whereas for the UN-AlNPs, the oxide layer has been found to be fully adhered to the core.[31] As the temperature approaches the melting point of aluminum (933 K), depending on the stress level and delamination in the core, fractures and the removal of delaminated parts of the shell are likely to happen, leading to the formation of a large number of tiny cracks in the alumina layer. Such a phenomenon is negligible in the UN-AlNPs, where the extent of shell failure is the least, and with the more or less intact oxide shell, a larger share of oxygenated products

has been formed even up to 1050 K.[36] In the SA-AlNPs, the molten aluminum leaks through the holes created in the thinner oxide layer and occupies a significant surface area of the alumina shell (Scheme 2)—explaining the less available reactive oxidizer surface, yielding a decreased amount of oxygenated species compared to that of the UN-AlNPs. In contrast, the early release of molten aluminum provides a large specific surface area-to-volume ratio and acts as an excellent heat conductor (thermal conductivity of AlNPs = 237 W m$^{-1}$ K$^{-1}$)[59] compared to the insulator material, alumina. This enhanced surface area and superior heat transfer by the metallic aluminum increase the contact time with the JP-10 vapor and facilitate the extent of thermal energy transfer to the parent molecule for the initial C−H bond cleavage to occur at lower temperatures.

Upon approaching the terminal decomposition temperature (1350 K), the Al core expands further with simultaneous widening of the cracks, resulting in a larger passage of molten aluminum, which effectively covers the whole oxide layer surface for the SA-AlNPs. Hence, at elevated temperatures, the metallic aluminum can react with the alumina shell, transforming it into a suboxide-dominated layer.[60−62] As aluminum monoxide (AlO) has not been detected in the gas phase here, unlike in the case of UN-AlNPs, it is possible that the transient suboxides (AlO, AlO$_2$, and Al$_2$O$_2$) remain chemisorbed on the alumina wrapping the NPs,[63] followed by reactions with the adsorbed JP-10 at the interface. By abstracting the hydrogen atom from one of the C−H bonds of the parent molecule, it can form C$_{10}$H$_{15}$ radicals, which serve as the precursors of the closed- and open-shell hydrocarbons.[19,36] For example, AlO reacts with JP-10 (C$_{10}$H$_{16}$) to form six distinct JP-10 carbon-centered radicals (C$_{10}$H$_{15}$) and aluminum monohydroxide (AlOH), which are exoergic in the range of 52 to 98 kJ mol$^{-1}$ with a low barrier of the transition states spanning 4 to 20 kJ mol$^{-1}$ above the separated reactants.[64] Besides the catalytic thermal conductivity by aluminum, there could be complementary chemical activation of the hydrocarbon fuel[65,66] (JP-10) molecules by the metal itself. Aluminum can abstract the hydrogen atom from JP-10 to form C$_{10}$H$_{15}$ radicals via endothermic pathways[18] with reaction enthalpies of 102−142 kJ mol$^{-1}$, and these channels are accessible with the abundant thermal energy available for the mentioned temperature range in the reactor. The closed-shell nascent hydrocarbon products can also undergo hydrogen atom abstraction, followed by dissociation on the surface to form smaller (C1−C4) hydrocarbon molecules and radicals, as realized by the greater branching ratio of the species for SA-AlNPs (36.4%) than that of the UN-AlNPs (20.6%).

At the maximum temperature (1350 K) and beyond, the NPs are thermodynamically driven to sinter,[60] thus producing characteristically larger particles with a lesser surface area, which limits the heterogeneous chemical interactions with the gas-phase hydrocarbon to some extent. Simultaneously, in this temperature range, the gas-phase decomposition channel of JP-10 involving collisions with helium atoms of the carrier gas also contributes significantly.[36,40] These two complementary reaction channels, overall, drive the reaction sequences to attain a lowered full decomposition temperature. In this high-temperature range, the formation of the simplest five-membered cyclic hydrocarbons can occur in the gas phase via the C−C bond β-scission of the hydrogen-abstracted JP-10 (C$_{10}$H$_{15}$) radicals, followed by ring opening and isomerization leading to cyclopentyl (C$_5$H$_7$) and cyclopentene (C$_5$H$_8$) with a barrier of only 168 kJ mol$^{-1}$.[40]

## 4. CONCLUSIONS

To summarize, the present work represents distinct reactivities of AlNPs upon stress-altering treatment toward the hydrocarbon jet fuel, JP-10, by probing the stable products as well as the intermediates formed in situ, both qualitatively and quantitatively. The pretreated AlNPs exhibit delayed initial reactivity in the low-temperature regime compared to that of the UN particles owing to the decreased surface energy in the former, leading to diminished reactivity of the alumina shell. Throughout the temperature range (850−1350 K), a smaller fraction of the oxygenated products provides evidence on the suppressed reactivity of the alumina layer—the sole source of oxygen. The imperfections generated in the alumina shell near the melting point of aluminum due to the elevated stress level allow the leakage of the molten core material instead of violent spallation, and the exposed molten aluminum layer serves as an excellent heat conductor to supply the thermal energy for the initial decomposition of JP-10. Moreover, the released metallic core is supposed to form an interfacial suboxide layer upon reacting with the alumina shell, which facilitates the hydrogen atom abstraction from the C−H bonds of JP-10, enhancing the decomposition of the precursor. The early onset of the full decomposition of the fuel by SA-AlNPs with 100 and 250 K lower temperatures compared to the UN-AlNPs and the pyrolysis without any additive, respectively, is a consequence of extensive surface-mediated dissociative fragmentation, which is supported by the detection of a large fraction of small-sized open- and closed-shell hydrocarbons at the high-temperature ranges. This study offers an in-depth understanding of temperature-dependent intrinsic catalytic interactions between metal NPs (AlNPs) and hydrocarbon fuel molecules (JP-10) and also evokes an understanding of the diverse surface properties of these particles to elucidate associated reaction behaviors. Overall, the pretreatment of the SA-AlNPs has been found to be a cost-effective method for making them more efficient and suitable than the UN-AlNPs for application in air breathing propulsion systems as jet fuel additives. The results here motivate further investigations involving metal particles to provide insights on reaction mechanisms that contribute to energy conversion in different environments.

## ■ ASSOCIATED CONTENT

### ⓢ Supporting Information

The Supporting Information is available free of charge at https://pubs.acs.org/doi/10.1021/acs.jpca.4c02023.

> Schematic of the experimental setup including the catalytic microreactor and reflectron time-of-flight mass spectrometer; PIE curves for the products formed at 850 and 1050 K; compilation of the products observed in the thermal decomposition of JP-10 on the UN- and SA-AlNPs; mass spectra recorded at 15.4 eV; temperature-dependent relative abundances of closed-shell hydrocarbons, hydrocarbon radicals, and oxygenated products; and comparison of the temperature-dependent relative abundances of the common hydrocarbon radicals formed upon thermal decomposition of JP-10 on the SA- and UN-AlNPs (PDF)

## AUTHOR INFORMATION

### Corresponding Authors

**Musahid Ahmed** − *Chemical Sciences Division, Lawrence Berkeley National Laboratory, Berkeley, California 94720, United States;* ⊚ orcid.org/0000-0003-1216-673X; Email: mahmed@lbl.gov

**Michelle L. Pantoya** − *Mechanical Engineering Department, Texas Tech University, Lubbock, Texas 79409, United States;* ⊚ orcid.org/0000-0003-0299-1832; Email: michelle.pantoya@ttu.edu

**Ralf I. Kaiser** − *Department of Chemistry, University of Hawai'i at Manoa, Honolulu, Hawaii 96822, United States;* ⊚ orcid.org/0000-0002-7233-7206; Email: ralfk@ hawaii.edu

### Authors

**Souvick Biswas** − *Department of Chemistry, University of Hawai'i at Manoa, Honolulu, Hawaii 96822, United States*

**Dababrata Paul** − *Department of Chemistry, University of Hawai'i at Manoa, Honolulu, Hawaii 96822, United States*

**Nureshan Dias** − *Chemical Sciences Division, Lawrence Berkeley National Laboratory, Berkeley, California 94720, United States*

**Kallista Kunzler** − *Mechanical Engineering Department, Texas Tech University, Lubbock, Texas 79409, United States*

Complete contact information is available at:
https://pubs.acs.org/10.1021/acs.jpca.4c02023

### Notes

The authors declare no competing financial interest.

## REFERENCES

(1) Mursalat, M.; Huang, C.; Julien, B.; Schoenitz, M.; Esteve, A.; Rossi, C.; Dreizin, E. L. Low-Temperature Exothermic Reactions in Al/CuO Nanothermites Producing Copper Nanodots and Accelerating Combustion. *ACS Appl. Nano Mater.* **2021**, *4*, 3811−3820.

(2) Jiang, Y.; Deng, S.; Hong, S.; Zhao, J.; Huang, S.; Wu, C.-C.; Gottfried, J. L.; Nomura, K.-i.; Li, Y.; Tiwari, S.; et al. Energetic Performance of Optically Activated Aluminum/Graphene Oxide Composites. *ACS Nano* **2018**, *12*, 11366−11375.

(3) Trunov, M. A.; Schoenitz, M.; Zhu, X.; Dreizin, E. L. Effect of Polymorphic Phase Transformations in Al$_2$O$_3$ Film on Oxidation Kinetics of Aluminum Powders. *Combust. Flame* **2005**, *140*, 310−318.

(4) Dreizin, E. L. Metal-Based Reactive Nanomaterials. *Prog. Energy Combust. Sci.* **2009**, *35*, 141−167.

(5) Gesner, J.; Pantoya, M. L.; Levitas, V. I. Effect of Oxide Shell Growth on Nano-Aluminum Thermite Propagation Rates. *Combust. Flame* **2012**, *159*, 3448−3453.

(6) Miller, K. K.; Gottfried, J. L.; Walck, S. D.; Pantoya, M. L.; Wu, C.-C. Plasma Surface Treatment of Aluminum Nanoparticles for Energetic Material Applications. *Combust. Flame* **2019**, *206*, 211−213.

(7) Rizzo, G. L.; Biswas, S.; Antonov, I.; Miller, K. K.; Pantoya, M. L.; Kaiser, R. I. Exotic Inverse Kinetic Isotopic Effect in the Thermal Decomposition of Levitated Aluminum Iodate Hexahydrate Particles. *J. Phys. Chem. Lett.* **2023**, *14*, 2722−2730.

(8) Keshavarz, M. H. *Liquid Fuels as Jet Fuels and Propellants: A Review of Their Productions and Applications*; Nova Science Publishers: New York, 2018.

(9) Jing, Q.; Wang, D.; Shi, C. Effects of Aluminum Powder Additives on Deflagration And Detonation Performance of JP-10/DEE Mixed Fuel under Weak and Strong Ignition Conditions. *Appl. Energy* **2023**, *331*, 120477.

(10) Luo, Y.; Xu, X.; Zou, J.-J.; Zhang, X. Combustion of JP-10-Based Slurry with Nanosized Aluminum Additives. *J. Propul. Power* **2016**, *32*, 1167−1177.

(11) Liu, L.; Zhang, Q.; Shen, S.; Li, D.; Lian, Z.; Wang, Y. Evaluation of Detonation Characteristics of Aluminum/JP-10/Air Mixtures at Stoichiometric Concentrations. *Fuel* **2016**, *169*, 41−49.

(12) Liu, J. Z.; Chen, B. H.; Wu, T. T.; Yang, W. J.; Zhou, J. H. Ignition and Combustion Characteristics and Agglomerate Evolution Mechanism of Aluminum in nAl/JP-10 Nanofluid Fuel. *J. Therm. Anal.* **2019**, *137*, 1369−1379.

(13) Chen, B. H.; Liu, J. Z.; Li, H. P.; Yang, W. J.; Cen, K. F. Laser Ignition and Combustion Characteristics of Al/JP-10 Nanofluid Droplet. *J. Therm. Anal.* **2019**, *135*, 925−934.

(14) E, X.-T.-F.; Zhang, L.; Wang, F.; Zhang, X.; Zou, J.-J. Synthesis of Aluminum Nanoparticles as Additive to Enhance Ignition and Combustion of High Energy Density Fuels. *Front. Chem. Sci. Eng.* **2018**, *12*, 358−366.

(15) E, X.-T.-F.; Pan, L.; Wang, F.; Wang, L.; Zhang, X.; Zou, J.-J. Al-Nanoparticle-Containing Nanofluid Fuel: Synthesis, Stability, Properties, and Propulsion Performance. *Ind. Eng. Chem. Res.* **2016**, *55*, 2738−2745.

(16) Javed, I.; Baek, S. W.; Waheed, K. Autoignition and Combustion Characteristics of Heptane Droplets with the Addition of Aluminium Nanoparticles at Elevated Temperatures. *Combust. Flame* **2015**, *162*, 191−206.

(17) Allen, C.; Mittal, G.; Sung, C.-J.; Toulson, E.; Lee, T. An Aerosol Rapid Compression Machine for Studying Energetic-Nanoparticle-Enhanced Combustion of Liquid Fuels. *Proc. Combust. Inst.* **2011**, *33*, 3367−3374.

(18) Brotton, S. J.; Malek, M. J.; Anderson, S. L.; Kaiser, R. I. Effects of Acetonitrile-Assisted Ball-Milled Aluminum Nanoparticles on the Ignition of Acoustically Levitated exo-Tetrahydrodicyclopentadiene (JP-10) Droplets. *Chem. Phys. Lett.* **2020**, *754*, 137679.

(19) Lucas, M.; Brotton, S. J.; Min, A.; Woodruff, C.; Pantoya, M. L.; Kaiser, R. I. Effects of Size and Prestressing of Aluminum Particles on the Oxidation of Levitated exo-Tetrahydrodicyclopentadiene Droplets. *J. Phys. Chem. A* **2020**, *124*, 1489−1507.

(20) Lucas, M.; Brotton, S. J.; Min, A.; Pantoya, M. L.; Kaiser, R. I. Oxidation of Levitated exo-Tetrahydrodicyclopentadiene Droplets Doped with Aluminum Nanoparticles. *J. Phys. Chem. Lett.* **2019**, *10*, 5756−5763.

(21) Rizzo, G. L.; Biswas, S.; Pantoya, M. L.; Kaiser, R. I. Unraveling the Ignition Chemistry of Singly Levitated Aluminum Iodate Hexahydrate (AIH) Particles. *Chem. Phys. Lett.* **2024**, *842*, 141212.

(22) Wang, W.; Li, H.; Zhang, M.; Zhao, F.; Xu, S.; Wang, C.; Qin, Z.; An, T.; Xu, K. Effects of Oxidizer and Architecture on the Thermochemical Reactivity, Laser Ignition and Combustion Properties of Nanothermite. *Fuel* **2022**, *314*, 123141.

(23) Wang, H.; Kline, D. J.; Biswas, P.; Zachariah, M. R. Connecting Agglomeration and Burn Rate in a Thermite Reaction: Role of Oxidizer Morphology. *Combust. Flame* **2021**, *231*, 111492.

(24) Chen, Y.; Ren, W.; Zheng, Z.; Wu, G.; Hu, B.; Chen, J.; Wang, J.; Yu, C.; Ma, K.; Zhou, X.; et al. Reactivity Adjustment from the Contact Extent between CuO and Al Phases in Nanothermites. *Chem. Eng. J.* **2020**, *402*, 126288.

(25) Wang, X.; Wu, T.; Zachariah, M. R. Doped Perovskites To Evaluate the Relationship between Fuel-Oxidizer Thermite Ignition and Bond Energy, Electronegativity, and Oxygen Vacancy. *J. Phys. Chem. C* **2017**, *121*, 147−152.

(26) Hill, K. J.; Tamura, N.; Levitas, V. I.; Pantoya, M. L. Impact Ignition and Combustion of Micron-Scale Aluminum Particles Pre-Stressed with Different Quenching Rates. *J. Appl. Phys.* **2018**, *124*, 115903.

(27) Jacob, R. J.; Hill, K. J.; Yang, Y.; Pantoya, M. L.; Zachariah, M. R. Pre-Stressing Aluminum Nanoparticles as a Strategy to Enhance reactivity of Nanothermite Composites. *Combust. Flame* **2019**, *205*, 33−40.

(28) Williams, A.; Shancita, I.; Vaz, N. G.; Tran-Ngo, T.; Demko, A.; Altman, I.; Hill, K. J.; Tunega, D.; Aquino, A. J. A.; Pantoya, M. L. Stress-Altered Aluminum Powder Dust Combustion. *J. Appl. Phys.* **2020**, *127*, 175110.

(29) Hill, K. J.; Warzywoda, J.; Pantoya, M. L.; Levitas, V. I. Dropping the Hammer: Examining Impact Ignition and Combustion Using Pre-Stressed Aluminum Powder. *J. Appl. Phys.* **2017**, *122*, 125102.

(30) Hill, K. J.; Pantoya, M. L.; Washburn, E.; Kalman, J. Single Particle Combustion of Pre-Stressed Aluminum. *Materials* **2019**, *12*, 1737.

(31) Bello, M. N.; Williams, A. M.; Levitas, V. I.; Tamura, N.; Unruh, D. K.; Warzywoda, J.; Pantoya, M. L. Highly Reactive Energetic Films by Pre-Stressing Nano-Aluminum Particles. *RSC Adv.* **2019**, *9*, 40607−40617.

(32) Firmansyah, D. A.; Sullivan, K.; Lee, K.-S.; Kim, Y. H.; Zahaf, R.; Zachariah, M. R.; Lee, D. Microstructural Behavior of the Alumina Shell and Aluminum Core Before and After Melting of Aluminum Nanoparticles. *J. Phys. Chem. C* **2012**, *116*, 404−411.

(33) Levitas, V. I.; Pantoya, M. L.; Chauhan, G.; Rivero, I. Effect of the Alumina Shell on the Melting Temperature Depression for Aluminum Nanoparticles. *J. Phys. Chem. C* **2009**, *113*, 14088−14096.

(34) Levitas, V. I.; Pantoya, M. L.; Dikici, B. Melt Dispersion versus Diffusive Oxidation Mechanism for Aluminum Nanoparticles: Critical Experiments and Controlling Parameters. *Appl. Phys. Lett.* **2008**, *92*, 011921.

(35) Sundaram, D. S.; Puri, P.; Yang, V. A General Theory of Ignition and Combustion of Nano- And Micron-Sized Aluminum Particles. *Combust. Flame* **2016**, *169*, 94−109.

(36) Biswas, S.; Paul, D.; He, C.; Dias, N.; Ahmed, M.; Pantoya, M. L.; Kaiser, R. I. Counterintuitive Catalytic Reactivity of the Aluminum Oxide "Passivation" Shell of Aluminum Nanoparticles Facilitating the Thermal Decomposition of *exo*-Tetrahydrodicyclopentadiene (JP-10). *J. Phys. Chem. Lett.* **2023**, *14*, 9341−9350.

(37) Shancita, I.; Altman, I.; Burnett, D.; Zorrilla, E. G.; Garcia, A. R.; Hill, K.; Pantoya, M. Demonstrating an Altered Metal Oxidation Reaction Mechanism Correlated with Variations in Surface Energy. *Thermochim. Acta* **2023**, *725*, 179521.

(38) Kohn, D. W.; Clauberg, H.; Chen, P. Flash Pyrolysis Nozzle for Generation of Radicals in a Supersonic Jet Expansion. *Rev. Sci. Instrum.* **1992**, *63*, 4003−4005.

(39) Zhang, F.; Kaiser, R. I.; Golan, A.; Ahmed, M.; Hansen, N. A VUV Photoionization Study of the Combustion-Relevant Reaction of the Phenyl Radical (C6H5) with Propylene (C3H6) in a High Temperature Chemical Reactor. *J. Phys. Chem. A* **2012**, *116*, 3541−3546.

(40) Zhao, L.; Yang, T.; Kaiser, R. I.; Troy, T. P.; Xu, B.; Ahmed, M.; Alarcon, J.; Belisario-Lara, D.; Mebel, A. M.; Zhang, Y.; et al. A Vacuum Ultraviolet Photoionization Study on High-Temperature Decomposition of JP-10 (*exo*-Tetrahydrodicyclopentadiene). *Phys. Chem. Chem. Phys.* **2017**, *19*, 15780−15807.

(41) Parker, D. S. N.; Kaiser, R. I. On the Formation of Nitrogen-Substituted Polycyclic Aromatic Hydrocarbons (NPAHs) in Circum-stellar and Interstellar Environments. *Chem. Soc. Rev.* **2017**, *46*, 452−463.

(42) NSRL. *Photoionization Cross Section Database (Version 2.0)*; National Synchrotron Radiation Laboratory: Hefei, China, 2023. accessed October 11, 2023. http://flame.nsrl.ustc.edu.cn/database/.

(43) Kaiser, R. I.; Zhao, L.; Lu, W.; Ahmed, M.; Krasnoukhov, V. S.; Azyazov, V. N.; Mebel, A. M. Unconventional Excited-State Dynamics

in the Concerted Benzyl (C7H7) Radical Self-Reaction to Anthracene (C14H10). *Nat. Commun.* **2022**, *13*, 786.

(44) Zhang, T.; Tang, X. N.; Lau, K. C.; Ng, C. Y.; Nicolas, C.; Peterka, D. S.; Ahmed, M.; Morton, M. L.; Ruscic, B.; Yang, R.; et al. Direct Identification of Propargyl Radical in Combustion Flames by Vacuum Ultraviolet Photoionization Mass Spectrometry. *J. Chem. Phys.* **2006**, *124*, 074302.

(45) Huang, C.; Wei, L.; Yang, B.; Wang, J.; Li, Y.; Sheng, L.; Zhang, Y.; Qi, F. Lean Premixed Gasoline/Oxygen Flame Studied with Tunable Synchrotron Vacuum UV Photoionization. *Energy Fuels* **2006**, *20*, 1505−1513.

(46) Meloni, G.; Selby, T. M.; Goulay, F.; Leone, S. R.; Osborn, D. L.; Taatjes, C. A. Photoionization of 1-Alkenylperoxy and Alkylperoxy Radicals and a General Rule for the Stability of Their Cations. *J. Am. Chem. Soc.* **2007**, *129*, 14019−14025.

(47) Savee, J. D.; Sztáray, B.; Welz, O.; Taatjes, C. A.; Osborn, D. L. Valence Photoionization and Autoionization of the Formyl Radical. *J. Phys. Chem. A* **2021**, *125*, 3874−3884.

(48) Qi, F. E. I.; McIlroy, A. Identifying Combustion Intermediates via Tunable Vacuum Ultraviolet Photoionization Mass Spectrometry. *Combust. Sci. Technol.* **2005**, *177*, 2021−2037.

(49) Parker, D. S. N.; Kaiser, R. I.; Troy, T. P.; Kostko, O.; Ahmed, M.; Mebel, A. M. Toward the Oxidation of the Phenyl Radical and Prevention of PAH Formation in Combustion Systems. *J. Phys. Chem. A* **2015**, *119*, 7145−7154.

(50) Wu, X.; Zhou, X.; Hemberger, P.; Bodi, A. The Ionization Energy of the Vinyl Radical: A Mexican Standoff with a Happy Ending. *Phys. Chem. Chem. Phys.* **2019**, *21*, 22238−22247.

(51) Prendergast, M. B.; Kirk, B. B.; Savee, J. D.; Osborn, D. L.; Taatjes, C. A.; Hemberger, P.; Blanksby, S. J.; da Silva, G.; Trevitt, A. J. Product Detection Study of the Gas-Phase Oxidation of Methylphenyl Radicals Using Synchrotron Photoionisation Mass Spectrometry. *Phys. Chem. Chem. Phys.* **2019**, *21*, 17939−17949.

(52) Rabalais, J. W.; Debies, T. P.; Berkosky, J. L.; Huang, J. T. J.; Ellison, F. O. Calculated Photoionization Cross Sections and Relative Experimental Photoionization Intensities for a Selection of Small Molecules. *J. Chem. Phys.* **1974**, *61*, 516−528.

(53) Page, R. H.; Larkin, R. J.; Shen, Y. R.; Lee, Y. T. High-Resolution Photoionization Spectrum of Water Molecules in a Supersonic Beam. *J. Chem. Phys.* **1988**, *88*, 2249−2263.

(54) Berkowitz, J.; Greene, J. P.; Cho, H.; Ruscic, B. The Ionization Potentials of CH4 and CD4. *J. Chem. Phys.* **1987**, *86*, 674−676.

(55) Yuan, W.; Zhao, L.; Yang, J.; Zhou, Z.; Li, Y.; Qi, F. Insights into the Decomposition and Oxidation Chemistry of p-Xylene in Laminar Premixed Flames. *J. Phys. Chem. A* **2021**, *125*, 3189−3197.

(56) Sun, W.; Hamadi, A.; Ardila, F. E. C.; Abid, S.; Chaumeix, N.; Comandini, A. Insights into Pyrolysis Kinetics of Xylene Isomers behind Reflected Shock Waves. *Combust. Flame* **2022**, *244*, 112247.

(57) Zhang, Z.; Liu, T.; Smith, A. E.; Medhekar, N. V.; Nakashima, P. N. H.; Bourgeois, L. Mechanisms of Void Shrinkage in Aluminium. *J. Appl. Crystallogr.* **2016**, *49*, 1459−1470.

(58) Altman, I.; Demko, A.; Hill, K.; Pantoya, M. On the Possible Coexistence of Two Different Regimes of Metal Particle Combustion. *Combust. Flame* **2020**, *221*, 416−419.

(59) Murshed, S. M. S. Simultaneous Measurement of Thermal Conductivity, Thermal Diffusivity, and Specific Heat of Nanofluids. *Heat Transfer Eng.* **2012**, *33*, 722−731.

(60) Chakraborty, P.; Zachariah, M. R. Do Nanoenergetic Particles Remain Nano-Sized during Combustion? *Combust. Flame* **2014**, *161*, 1408−1416.

(61) Starik, A. M.; Savel'ev, A. M.; Titova, N. S. Specific Features of Ignition and Combustion of Composite Fuels Containing Aluminum Nanoparticles (Review). *Combust. Explos. Shock Waves* **2015**, *51*, 197−222.

(62) Cochran, C. N. Aluminum Suboxide Formed in Reaction of Aluminum with Alumina. *J. Am. Chem. Soc.* **1955**, *77*, 2190−2191.

(63) Storozhev, V. B.; Yermakov, A. N. Effect of Suboxides on Dynamics of Combustion of Aluminum Nanopowder In Water Vapor: Numerical Estimate. *Combust. Flame* **2018**, *190*, 103−111.

(64) Brotton, S. J.; Perera, S. D.; Misra, A.; Kleimeier, N. F.; Turner, A. M.; Kaiser, R. I.; Palenik, M.; Finn, M. T.; Epshteyn, A.; Sun, B.-J.; et al. Combined Spectroscopic and Computational Investigation on the Oxidation of exo-Tetrahydrodicyclopentadiene (JP-10; C10H16) Doped with Titanium-Aluminum-Boron Reactive Metal Nanopowder. *J. Phys. Chem. A* **2022**, *126*, 125−144.

(65) Sayed Ahmad, M.; Kritikos, E. M.; Giusti, A. A Reactive Molecular Dynamics Investigation of Nanoparticle Interactions in Hydrocarbon Combustion. *Combust. Sci. Technol.* **2023**, *195*, 3281−3295.

(66) Smirnov, V. V.; Kostritsa, S. A.; Kobtsev, V. D.; Titova, N. S.; Starik, A. M. Experimental Study of Combustion of Composite Fuel Comprising n-Decane and Aluminum Nanoparticles. *Combust. Flame* **2015**, *162*, 3554−3561.